Effect of Melt Superheat and Alloy Size on the Mixing Phenomena in Argon-Stirred Steel Ladles

Haojian Duan, Lifeng Zhang, and Brian G. Thomas*

In the current study, the melting and mixing behavior of the alloy in argon-stirred steel ladles is simulated based on the turbulent fluid flow. The formation of the solidified steel shells around cold ferroalloy particles is considered and the discrete phase model is adopted to predict the motion of ferroalloy particles. Ferroalloy particles are heated by the surrounding liquid during their travel trajectories and the mixing of dissolved alloy solute is described by the species transport model as the steel shell disappears. User defined functions are used to record the melting time and the trajectory length of each ferroalloy particle, as well as to check the mixing criteria in every cell and predict the local mixing time in the entire computational domain. Mixing time maps which visualize the mixing efficiency are obtained as a novel representation to describe the local mixing time in the entire ladle. The effects of the superheat of the melt and the diameter of alloy particles are investigated. The results show that the higher superheat of the melt and the smaller size of alloy particle facilitate the melting and mixing of the alloy in argon-stirred steel ladles.

1. Introduction

Alloying process is one of the main targets in steelmaking to overcome deleterious effects of other elements in the molten steel or to modify physical properties in the finished steel. A majority of bulk alloy additions are made to the ladle during tapping of the steel but there is a trend toward making more additions at the ladle furnace. Argon-stirred ladles are commonly used in the secondary refining[1] to homogenize chemical compositions and the temperature[2–5], to remove inclusions,[6,7] and to enhance the slag-metal reactions.[8–10] Many publications have been done to investigate the mixing phenomena in argon-stirred ladles experimentally[11–22] and numerically,[23–34] but less of them coupled the melting of alloy particles.

Mixing time has commonly been used to represent the state of agitation in gas-stirred ladles. Several empirical relationships[24,35,36] between mixing time and stirring energy have been reported. Nakanishi et al.[35] were among the first to plot experimental data on mixing time against energy dissipation rates for water models of argon-stirred ladles. Asai et al.[36] developed a correlation between mixing time and mixing power density from the view point of transport phenomena theoretically. Sano and Mori[37] correlated the mixing time as simple functions of gas flow rate, liquid depth, and cross-sectional areas of both the plume zone and the vessel based on a steady-state energy balance for the liquid phase. Mazumdar and Guthrie[24] summarized mixing time correlations reported in the literature under different experimental conditions, such as gas flow rates, vessel geometries, and nozzle configurations.

Water modeling[11–22] was usually adopted to study the hydrodynamics and mixing phenomena in gas stirred ladles. Murthy and Elliott[12] examined the definition of mixing time and analyzed the reported concentration vs. time traces to determine mixing time. Mazumdar et al.[17] studied the influence of ladle design on bath mixing as a function of gas flow rate, liquid depth, and gas injection configuration. Mandal et al.[16] carried out an experimental investigation on mixing phenomena in a ladles fitted with dual plugs. Kochi et al.[19] carried out an experiment to investigated the mixing time in a water bath agitated by side gas injection with an L-shaped lance. Ogawa and Onou[11] measured the mixing time and slag-metal masstransfer coefficient in gas bubbling and induction stirring by water model and plant scale experiments. Oils were used as top layers to simulate the slag phase in water models.[13–15,18,20–22] Yamashita et al.[15] carried out water model experiments to clarify the effect of the top oil layer on the mixing time in a bottom blown bath.

As an effective tool to understand the hydrodynamics, turbulence, and mixing phenomena in industrial ladles, computational modeling[23,34] is becoming more and more popular. Lee et al.[27] studied the fluid flow and mixing behavior in gas-stirred ladles with a submerged lance numerically. Ganguly et al.[32] investigated the effects of bubble slip phenomena in predicting the mixing time in gas-stirred ladles through a mathematical modeling procedure. Mazumdar et al.[29] investigated the transient flow and the mixing in steelmaking ladles during the initial period of gas stirring experimentally and numerically. Zhu et al.[25,26] conducted water

H. Duan, Prof. L. Zhang
School of Metallurgical and Ecological Engineering
University of Science and Technology Beijing (USTB)
Beijing 100083, China
E-mail: zhanglifeng@ustb.edu.cn

Prof. B. G. Thomas
Professor of Mechanical Engineering Colorado
School of Mines
Illinois Street 80401, Colorado

DOI: 10.1002/srin.201800288

model experiments and the three-dimensional numerical models to investigate the flow pattern and mixing phenomena in argon-stirred ladles with different types of tuyere arrangement. Turkoglu and Farouk[3,4] numerically studied the effects of bath aspect ratio and gas injection rate on mixing time and liquid circulation rate in steelmaking ladles with vertical gas injection. Jauhiainen et al.[28] studied the effect of porous plug location on alloy mixing theoretically using computational fluid dynamics modeling and reported that a centrically stirred ladle was very sensitive to alloy addition location. Maldonado-Parra et al.[33] suggested that mixing time was optimized with only one porous plug located at a radial position of 0.67 instead of two or three, while Lou and Zhu[7] recommended to use dual plugs with the radial position of 0.6R and the angle of 135°. Cloete et al.[34] implemented a mathematical model of a full scale gas stirred ladle in designed experiments to assess the effect of various design variables on mixing efficiency. Joo and Guthrie[23] and Madan et al.[31] studied the mixing phenomena in steelmaking ladles fitted with dual plugs using mathematical and aqueous physical models. Aoki et al.[30] investigated the three-dimensional multi-phase turbulent flow field and ferroalloy mixing in an off-centered gas-stirred ladle using plant measurements and computational models. Even though the melting time was considered in their numerical model, it is estimated to be a constant for a given superheat.

Taniguch et al.[38] investigated the effect of gas injection on the melting rate of solid sphere in a liquid bath and estimated heat and mass transfer coefficients by using a mathematical analysis. Zhang developed a mathematically model to investigate the melting process of sponge iron particles in iron-bath and derived a simplified analytical solution for the system in 1996[39] and a mathematically model for melting of ferro-manganese particles in liquid iron in a ladle and calculated the particle melting time analytically in 1999.[40] Besides, the melting and dissolution of low-density ferro-molybdenum and high-melting alloys in steel melts were also modeled by Zhang and Oeters.[41,42]

The fluid flow and mixing phenomena in argon-stirred steel ladles were simulated in our previous study and the effects of gas flow rate, porous plug location, and separation angle of two porous plugs were investigated.[43] In the current study, the effects of the superheat of the melt and the diameter of alloy particle on the melting and mixing phenomena of the ferrroalloy is investigated. The description of the mathematical model is presented in Section 2 and the melting and mixing process of the alloy is discussed in Section 3. Lastly, the effects of the superheat of the melt and the diameter of alloy particles are investigated in Section 4.

2. Mathematical Model

2.1. Fluid Flow in Argon-Stirred Ladles

The fluid flow in argon-stirred ladles was predicted based on the Euler–Lagrange approach. The liquid phase flow was calculated by solving the unsteady Reynolds-averaged Navier–Stokes (RANS) conservation equations combined with the well-known standard k-ε two-equation turbulence model in an Eulerian frame of reference. The effects of interphase forces and the bubble-induced turbulence on the liquid phase flow were considered by the momentum source and the turbulent kinetic energy source. Discrete phase model was used to describe the motion of argon bubbles in the liquid steel. The motion of each bubble was solved by integrating the forces balance of the drag force, the buoyancy force, the virtual mass force, the lift force, and the pressure gradient force on it, which was written in a Lagrangian reference frame. The density and the diameter of bubbles were considered by calculating at each position according to the local static pressure and the temperature using the ideal gas law. In order to account for the effect of turbulence flow on the bubble trajectory, the discrete random walk model was adopted. The drag coefficient was from Kuo and Wallis; the lift coefficient and the virtual mass coefficient were set to 0.1 and 0.5, respectively. The detailed information can be found in previous publication.[43–45]

Figure 1 shows the predicted flow field in a 150 ton argon stirred ladle. Dimensions of the ladle employed in the current study are shown in **Table 1**, as well as the property parameters. Argon bubbles are injected from a porous plug located 0.68R radial position with the gas flow rate of 220 NL min^{-1}. It is observed that the classic recirculation flow pattern is generated by the argon injection from the porous plug located at ladle bottom. In addition, it is important to notice that the smallest velocities are reached at the ladle bottom opposite the location of the porous plug.

2.2. Melting of Ferroalloy Particles

The alloying process in the molten steel consists of two main steps: 1) melting of solid ferroalloy particles and 2) mixing of the dissolved alloy element. In the current study, FeMn containing 71.8 wt% Mn is used as the ferroalloy. According to previous studies,[40] a solidified steel shell is generated around solid ferroalloy particle as the cold particle is thrown into the molten steel. Inside the solidified shell, the ferroalloy melts firstly duo to its low liquidus temperature. After a certain time, the ferroalloy

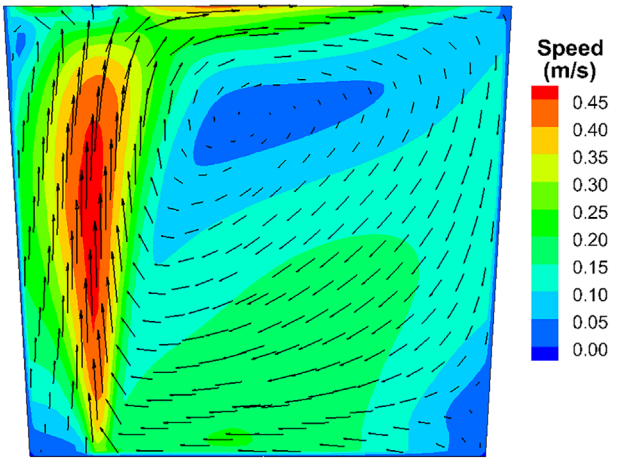

Figure 1. Predicted velocity field in the vertical plane of a 150 ton argon-stirred ladle with gas flow rate of 220 NL min^{-1} and porous plug location of 0.68R.

is nearly completely melted and hence, suddenly introduces into the molten steel when the shell has melted away, as shown in **Figure 2.**[39,40]

With the assumption that the resistance of heat transport in the solidified shell that initially coats at the particle surface is zero, the shell thickness and the particle melting time can be calculated analytically:

$$s = \begin{cases} \dfrac{\sqrt{\mathrm{Fo}d_A}}{\sqrt{\pi}\mathrm{Ph}(\rho_s/\rho_A)} - \dfrac{(\mathrm{Bi}\theta_M + 1)\mathrm{Fo}d_A}{2\mathrm{Ph}(\rho_s/\rho_A)} & \mathrm{Fo} < 1/\pi \\ \dfrac{d_A}{2\mathrm{Ph}(\rho_s/\rho_A)}\left(\dfrac{1}{\pi} - \mathrm{Bi}\theta_M\,\mathrm{Fo}\right) & \mathrm{Fo} \geq 1/\pi \end{cases} \quad (1)$$

$$t_s = \frac{\rho_A C_{p,A} d_A}{2\pi h \theta_M} \quad (2)$$

$$\theta_M = \frac{T_M - T_S}{T_S - T_0} \quad (3)$$

$$\mathrm{Fo} = \frac{4k_A t}{\rho_A C_{p,A} d_A^2} \quad (4)$$

$$\mathrm{Ph} = \frac{\Delta H_S}{C_{p,A}(T_S - T_0)} \quad (5)$$

$$\mathrm{Bi} = \frac{\mathrm{Nu}k_l}{2k_A} \quad (6)$$

Table 1. Ladle dimensions and property parameters employed in the current study.

Property	Symbol	Value	Unit
Top diameter of ladle		2.910	m
Bottom diameter of ladle		3.400	m
Height of ladle		4.200	m
Height of molten steel		2.870	m
Density of molten steel	ρ_l	7020	kg m^{-3}
Viscosity of molten steel	μ_l	0.0067	Pa · s
Heat capacity of liquid steel	$C_{p,M}$	820	J kg^{-1} K^{-1}
Thermal conductivity of liquid steel	k_M	40.3	J m^{-1} s^{-1} K^{-1}
Diffusion coefficient of the solute	D_M	5.5×10^{-5}	m^2 s^{-1}
Density of ferroalloy	ρ_A	6120	kg m^{-3}
Heat capacity of ferroalloy	$C_{p,A}$	845.7	J kg^{-1} K^{-1}
Thermal conductivity of ferroalloy	k_A	4.148	J m^{-1} s^{-1} K^{-1}
Density of solidified shell	ρ_S	7300	kg m^{-3}
Enthalpy change of melting of molten steel	ΔH_S	2.47×10^5	J kg^{-1}
Solidification temperature of molten steel	T_S	1803	K
Initial temperature of ferroalloy particle	T_0	298	K

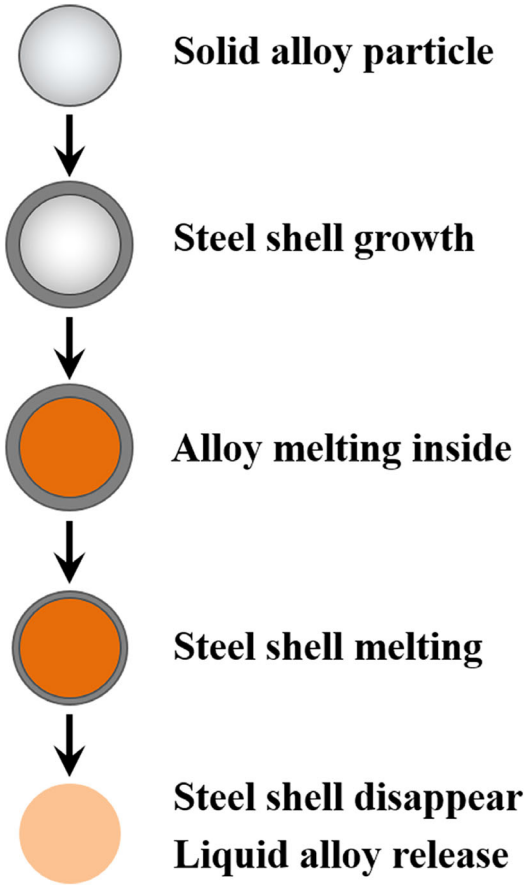

Figure 2. Melting of the FeMn alloy in molten steel.

$$h = \frac{\mathrm{Nu}k_M}{d_A} \quad (7)$$

$$\mathrm{Nu} = 2 + \left(0.4\mathrm{Re}^{1/2} + 0.06\mathrm{Re}^{2/3}\right)\mathrm{Pr}^{0.4} \quad (8)$$

$$\mathrm{Re} = \frac{\rho_l d_A (u_l - u_A)}{\mu_l} \quad (9)$$

$$\mathrm{Pr} = \frac{C_{p,M}\mu_l}{k_M} \quad (10)$$

where s is the thickness of the shell; t_S is the shell existence time; ρ_A, ρ_S, and ρ_l are the density of the ferroalloy, the shell and the molten steel, respectively; $C_{p,A}$ and $C_{p,M}$ is the heat capacity of the ferroalloy and the molten steel; d_A is the diameter of ferroalloy particle (m); θ_M is the dimensionless temperature; h is the heat transfer coefficient; ΔH_S is the enthalpy change of the melting of the shell; k_A and k_M are the thermal conductivity of the ferroalloy and the molten steel; μ_l is the molecular viscosity of molten steel;, and T_0 are the solidification temperature of the melt, the temperature of the melt and

the initial temperature of the ferroalloy particle, respectively; Bi, Fo, Nu, Ph, Pr, and Re are Biot number, Fourier number, Nusselt number, phase transfer number, Prandtl number, and Reynolds number, respectively.

2.3. Motion of Ferroalloy Particles

As discussed above, ferroalloy particles are coated by solidified steel shells when they are thrown into the molten steel. Thus, discrete phase model (DPM) is also used to predict the motion of ferroalloy particles and ferroalloy particles are treated as spherical particles. Trajectories of the ferroalloy particles are calculated from the computed velocity field by integrating the following particle velocity equation, which considers the force balance acting on the particles:

$$\frac{du_{A,i}}{dt} = \left\{ \begin{array}{l} \dfrac{\rho_{A,i} - \rho_l}{\rho_{A,i}} g + \dfrac{18\mu_l C_{D,i}\ \mathrm{Re_i}}{24 \mathrm{d}_{\mathrm{A,i}}^2 \rho_{\mathrm{A,i}}} \left(u_l - u_{A,l}\right) \\ + \dfrac{1}{2}\dfrac{\rho_l}{\rho_{A,i}} \dfrac{d}{dt}\left(u_l - u_{A,i}\right) + \dfrac{\rho_l}{\rho_{A,i}} u_l \cdot \nabla \cdot u_l \end{array} \right\} \tag{11}$$

Ferroalloy particles are assumed to be spherical and the spherical drag law is applied:

$$C_{D,A} = a_1 + \frac{a_2}{\mathrm{Re}_A} + \frac{a_3}{\mathrm{Re}_A^2} \tag{12}$$

where the constants a_1, a_2, and a_3 are given by Morsi and Alexander.[46]

The "stochastic" effect of turbulent fluctuations on the particle motion is also considered by the "random walk" model in which the liquid velocity fluctuations are based on a Gaussian-distributed random number, chosen according to the local turbulent kinetic energy.

2.4. Mixing of Alloy Solute

As the steel shell disappears, the mixing of alloy solute is described by the species transport model:

$$\frac{\partial}{\partial t}(\rho C) + \nabla \cdot (\rho u C) = \nabla \cdot \left(\rho D_M + \frac{\mu_t}{Sc_t}\right) \nabla C \tag{13}$$

where C is the local mass fraction of the alloy element; D_M is the diffusion coefficient of the alloy element ($\mathrm{m^2\,s^{-1}}$); and Sc_t is the turbulent Schmidt number defined as 0.7.

The mixing process in argon-stirred ladles could be evaluated by the mixing time which is defined as that time during which the concentration of alloy element is reached within 5% deviation of the homogeneous value. The mixing criteria is checked and the local mixing time is recorded in every computational cell. Thus, the mixing time map for the entire ladle is obtained. The mixing time is only account for the transport of the solute in previous studies, while both the melting of the alloy particle and the mixing of the solute are considered in the definition of the mixing time in the present paper. In addition, the mixing time map for the entire ladle is predicted rather than that for several single points.

2.5. Computational Details

In the present study, the commercial CFD software Fluent 14.0 combined with user defined functions (UDFs) is used to simulate the melting and mixing of ferroalloy in argon-stirred ladles. The turbulent fluid flow in a 150 ton argon-stirred ladle as shown in Figure 1 is used. The ferroalloy is added in a 200 mm diameter circle region just above the porous plug at a constant rate of $72.54\,\mathrm{kg\,s^{-1}}$ for 6 s and the initial velocity of each ferroalloy particle entry into the molten steel is set to $6.26\,\mathrm{m\,s^{-1}}$ vertically downward, corresponding to a two-meter vertical free fall velocity. During each ferroalloy particle trajectory calculation, the melting time and the trajectory length are recorded using a UDF. Once melted, the ferroalloy particle turns into a mass source of Mn at the melting location and the species transport model applies. For the species transport model, the zero flux boundary condition is used at the top surface and bottom and side walls. After the solute Mn uniformly dissolves into the liquid steel, the homogeneous value of Mn equals to 0.2%. In order to evaluate the mixing time in the ladle, the mixing criteria is checked in every cell using the UDF and the local mixing time is predicted in the whole computational domain.

3. Melting and Mixing Process of Alloy

The ferroalloy melting and mixing process is shown in **Figure 3**. The superheat of melt is 60 K and the diameter of alloy particle is 30 mm. The blue spheres represent alloy particles and the normalized Mn concentration maps are used to visualize the transport of the alloy solute. The blue region demonstrates the higher concentration and the red region demonstrates the lower. Because alloy particles are thrown into the liquid steel with $6.26\,\mathrm{m\,s^{-1}}$ vertically downward, they will penetrate into the bulk of melt (Figure 3a). However, ferroalloy particles float up immediately after addition since the density of alloy is less than that of the molten steel. Carrying by the turbulent liquid flow, ferroalloy particles drift along the steel-slag interface and accumulate around the perimeter of the top surface opposite from the bubble plume (Figure 3b, c). Meantime, ferroalloy particles are heated by the surrounding liquid. The molten ferroalloy is suddenly introduced into the liquid and diffuses from the position where the steel shell disappears (Figure 3c, d). It then circulates in the ladle and mixes by turbulent diffusion. Clearly, the liquid flow has a significant influence on the mixing of the alloy and the transport of the dissolved alloy follows the recirculation loops of liquid flow (Figure 3e–j). Because dead zones are existed in the ladle and the mixing condition is bad in the dead zone, the dissolved solute diffuses slowly at the bottom of the ladle (Figure 3k). Eventually, the solute concentration approaches the full homogenization (Figure 3l).

It is novel for the present study to find a new representation to describe the local mixing time in the entire ladle using mixing

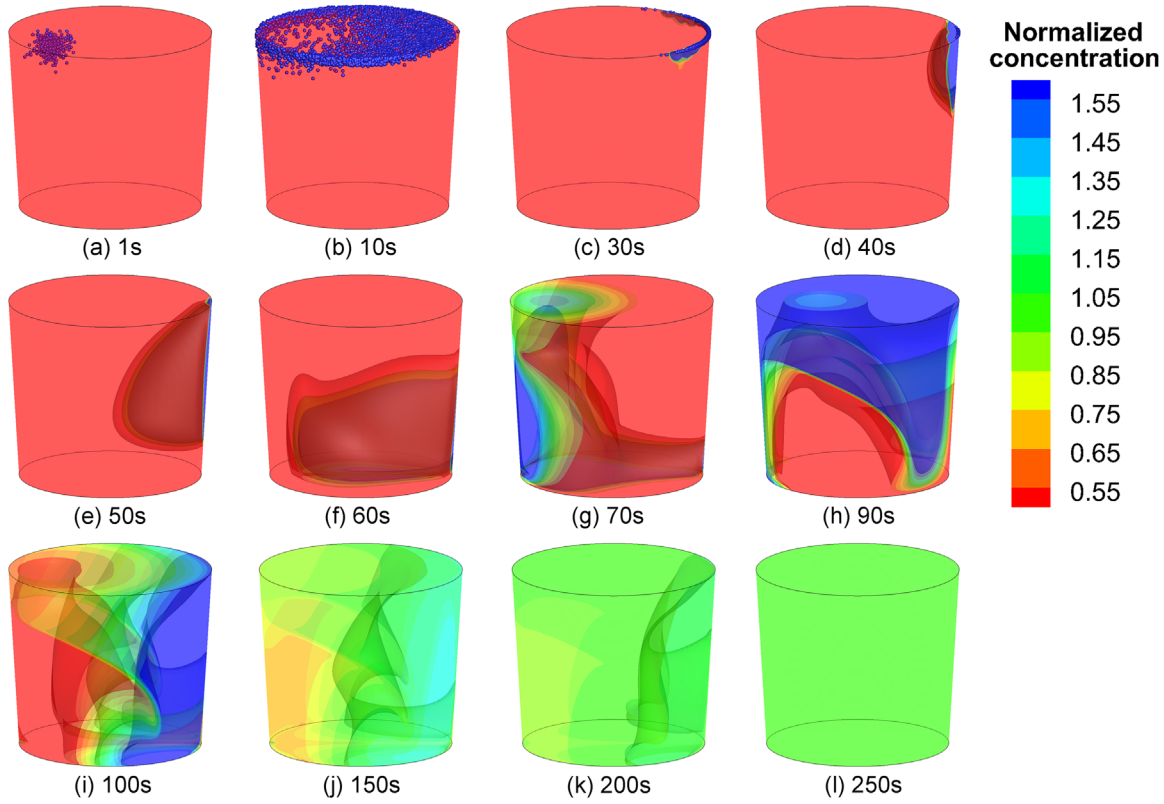

Figure 3. Melting and mixing of alloy in a 150 ton argon-stirred ladle with gas flow rate of 220 NL min^{-1} and porous plug location of 0.68R. The superheat of melt is 60 K and the diameter of alloy particle is 30 mm.

time maps. **Figure 4** shows the mixing time map in the vertical plane of a 150 ton argon-stirred ladle with gas flow rate of 220 NL min^{-1} and porous plug location of 0.68R. It can be observed a faster mixing process in the central region adjacent to the plume and a dead zone at the ladle bottom opposite from the plume. In the past, the previous research on mixing time only focused on the longest value of several points and ignored to describe the volume of liquid steel that reaches full

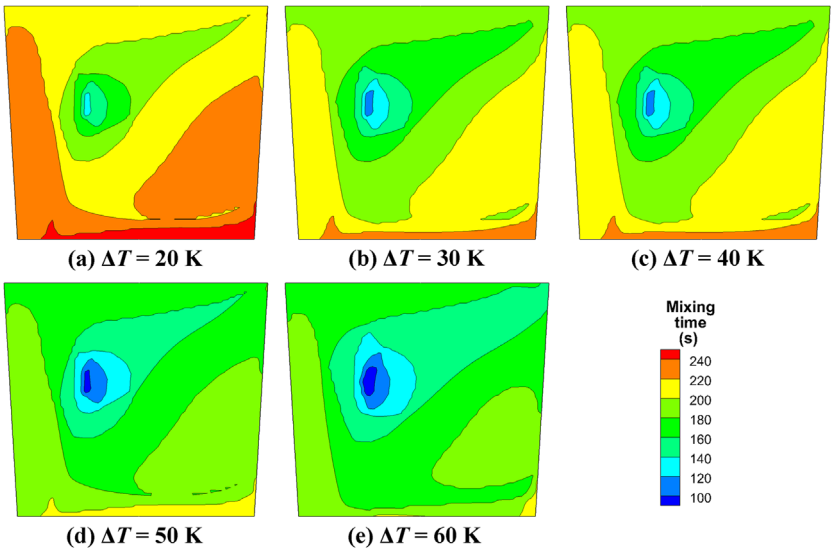

Figure 4. Predicted mixing time maps in the vertical plane of a 150 ton argon-stirred ladle for the superheat of a) 20 K, b) 30 K, c) 40 K, d) 50 K, and e) 60 K with the diameter of alloy particle of 30 mm.

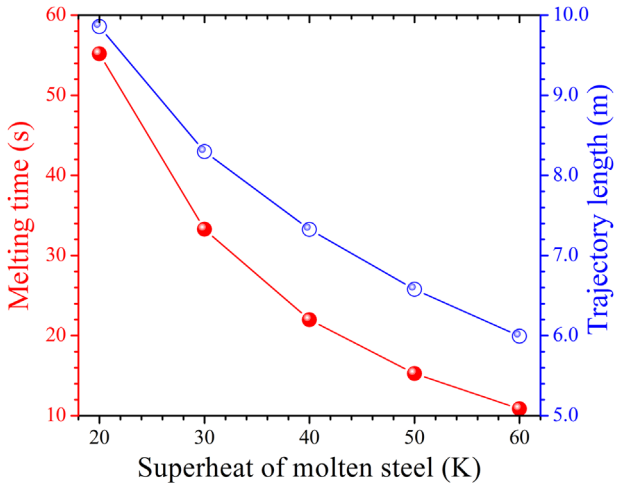

Figure 5. Effect of superheat on melting time and trajectory length in a 150 ton argon-stirred ladle with gas flow rate of 220 NL min^{-1} and porous plug location of 0.68R.

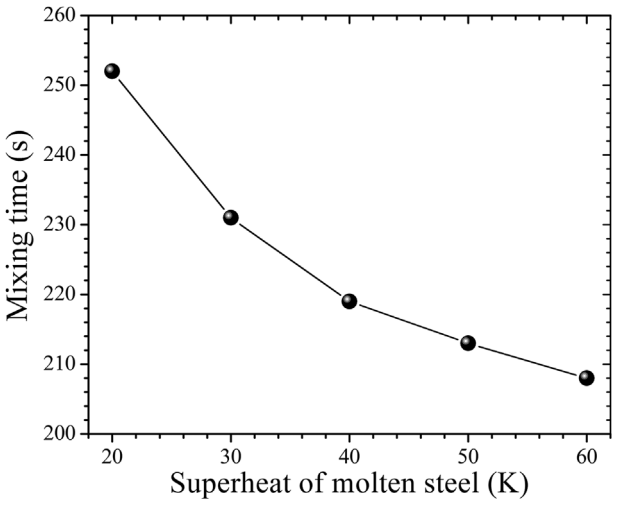

Figure 6. Effect of superheat on mixing time in a 150 ton argon-stirred ladle with gas flow rate of 220 NL min^{-1} and porous plug location of 0.68R.

homogenization. The mixing time map obtained in this study is useful because it can be used to define a new reference to improve the mixing process and promote a better understanding of the position of the dead zones in a ladle. The true mixing time is a single value for the entire steel ladle and this value corresponds to the maximum mixing time.

4. Parametric Study

4.1. Superheat of Molten Steel

The effect of superheat on the melting of alloy particles is shown in **Figure 5**. It is shown that the melting time of alloy particles decreases from 55.19 to 10.85 s and the trajectory length decreases from 9.86 to 5.99 m with an increment in the superheat from 20 to 60 K.

Figure 4 displays the predicted mixing time maps in the vertical plane of 150 ton ladles for different superheat. It can be observed the distribution of the mixing time almost similar: mixing faster near the bubble plume and slower at the ladle bottom opposite from the bubble plume. Even though the superheat of the melt has a great influence on the melting process of alloy particles, the mixing character is affected by the superheat limited, which also indicates that the liquid flow dominates the mixing process. **Figure 6** shows the maximum mixing time as a function of the superheat of the melt. It is also clearly shown a decrease in mixing time as the superheat increases, from 252 to 208 s by increasing the superheat from 20 to 60 K.

4.2. Diameter of Alloy Particle

Generally speaking, the smaller alloy particle melts faster than the bigger one. **Figure 7** shows the melting time and the trajectory length of alloy particles with different diameters. The solid line represents the superheat of 30 K and the dash line represents 60 K. As expected, both the melting time and the trajectory length are shorter for the smaller alloy particle whatever the superheat is. On the other hand, it can be seen that the melting time and the trajectory length increase faster for the superheat of 30 K than that for the superheat of 60 K with the increase of the diameter of alloy particle.

The predicted mixing time maps in the vertical plane of 150 ton ladles with different diameters of alloy particles is shown in **Figure 8**. The superheat of the melt is 30 K for (a–c) and 60 K for (d–f). Mixing time maps have similar distribution whatever the superheat of the melt and the diameter of alloy particles are. **Figure 9** shows the maximum mixing time as a function of the diameter of alloy particles. It is shown an increase in the mixing time as the diameter of alloy particle increases; from 200 to 231 s

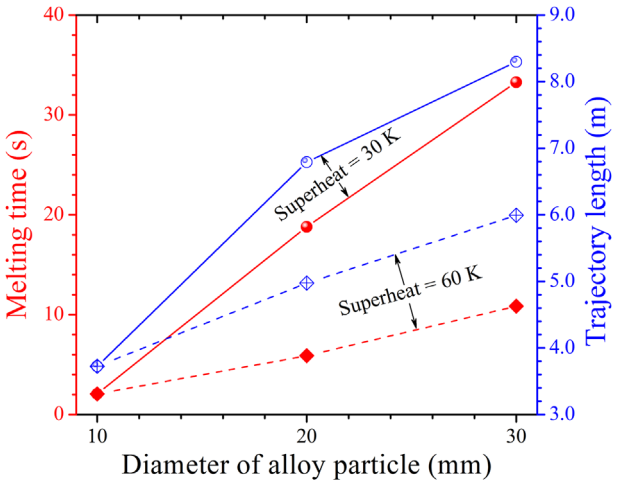

Figure 7. Effect of alloy particle diameter on melting time and trajectory length in a 150 ton argon-stirred ladle with gas flow rate of 220 NL min^{-1} and porous plug location of 0.68R.

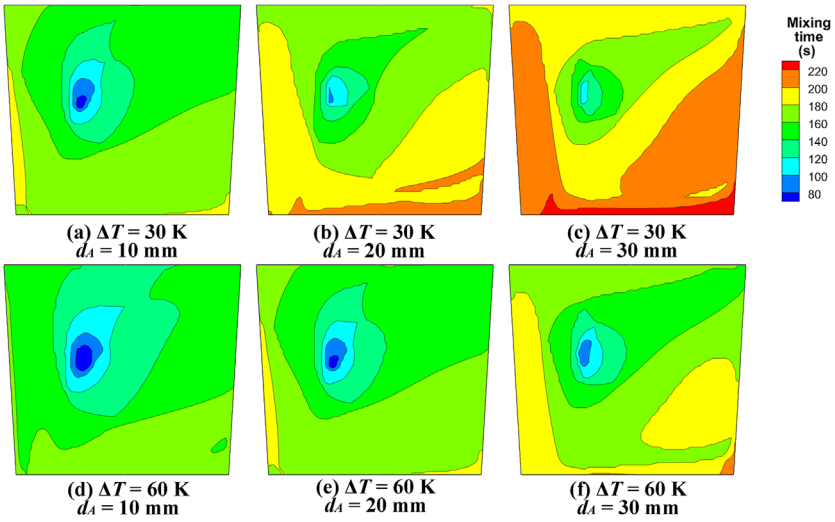

Figure 8. Predicted mixing time maps in the vertical plane of a 150 ton argon-stirred ladle with the diamter of alloy particle of a) 10 mm, b) 20 mm, and c) 30 mm for the superheat of 30 K and d) 10 mm, e) 20 mm, and f) 30 mm for the superheat of 60 K, respectively.

for the superheat of 30 K with an increment in the diameter of alloy particle from 10 to 30 mm and from 183 to 208 s for the superheat of 60 K.

5. Future Studies

It is assumed that the temperature field distributes uniformly in the ladle and the heat loss caused by the melting of alloy particles is ignored in the current study. Thus, the transient fluid flow and temperature distributions in argon-stirred ladles should be further investigated to couple the melting and mixing process in the future. Effect of the particle size distribution of alloy particle also should be considered in future studies since smaller alloy particles melt faster. The model presented here is an attempt to visualize to the melting and mixing of alloy in argon-stirred ladles and a rational experimental method should be established in the future to validate and modify the model developed in this study.

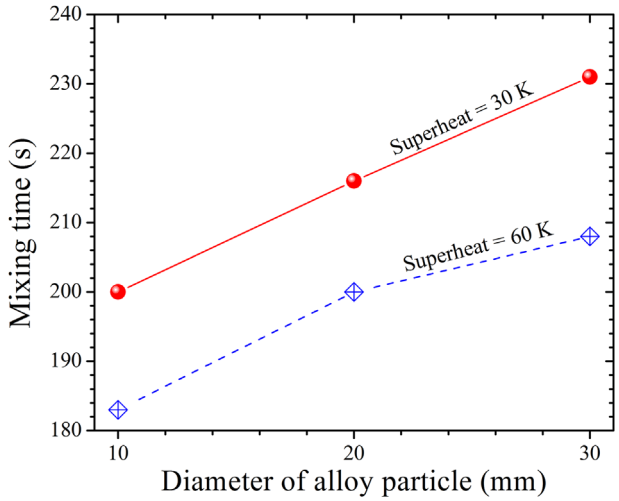

Figure 9. Effect of alloy particle diameter on mixing time in a 150 ton argon-stirred ladle with gas flow rate of 220 NL min^{-1} and porous plug location of 0.68R.

6. Conclusion

The melting and mixing behavior of the alloy in argon-stirred steel ladles is simulated. The discrete phase model is adopted to predict the motion of ferroalloy particles and the species transport model is employed to describe the mixing of dissolved alloy solute. The melting time and the trajectory length of ferroalloy particles are recorded by a user defined function. The mixing criteria in every computational cell is checked using the user defined function and the mixing time map is obtained as a novel way to describe the mixing condition in the entire ladle. Increasing the superheat of the melt, the melting and mixing of the alloy become faster. Smaller alloy particles melt and mix faster.

Acknowledgements

The authors were grateful for support from the National Science Foundation China (Grant No. 51725402), the Fundamental Research Funds for the Central Universities (Grant No. FRF-TP-15-001C2, No. FRF-TP-15-067A1, No. FRF-TP-17-039A1, and FRF-BD-17-010A), Beijing Key Laboratory of Green Recycling and Extraction of Metals (GREM) and the High Quality steel Consortium (HQSC) and Green Process Metallurgy and Modeling (GPM^2) at the School of Metallurgical and Ecological Engineering at University of Science and Technology Beijing (USTB), China.

Conflict of Interest

The authors declare no conflict of interest.

Keywords

alloy, argon-stirred steel ladles, melting, mixing

Received: June 4, 2018
Revised: August 2, 2018
Published online: August 30, 2018

[1] M. Salcudean, K. Y. M. Lai, R. I. L. Guthrie, *Can. J. Chem. Eng.* **1985**, *63*, 51.
[2] A. Castillejos, M. Salcudean, J. Brimacombe, *Metall. Trans. B* **1989**, *20*, 603.
[3] H. Turkoglu, B. Farouk, *Metall. Trans. B* **1990**, *21*, 771.
[4] H. Turkoglu, B. Farouk, *ISIJ Int.* **1991**, *31*, 1371.
[5] T. Hasmet, F. Bakhtier, *Numer. Heat Transfer Appl.* **1992**, *21*, 377.
[6] S. Mats, J. Pär, J. Lage, *Steel Res. Int.* **2004**, *75*, 128.
[7] W. Lou, M. Zhu, *ISIJ Int.* **2014**, *54*, 9.
[8] S. Kim, R. Fruehan, *Metall. Trans. B* **1987**, *18*, 381.
[9] G. Venturini, M. Goldschmit, *Metall. Mater. Trans. B* **2007**, *38*, 461.
[10] W. Lou, M. Zhu, *Metall. Mater. Trans. B* **2014**, *45*, 1706.
[11] K. Ogawa, T. Onoue, *ISIJ Int.* **1989**, *29*, 148.
[12] G. G. K. Murthy, J. F. Elliott, *ISIJ Int.* **1992**, *32*, 190.
[13] M. Iguchi, K.-I. Nakamura, R. Tsujino, *Metall. Mater. Trans. B* **1998**, *29*, 569.
[14] M. Iguchi, R. Tsujino, K.-I. Nakamura, M. Sano, *Metall. Mater. Trans. B* **1999**, *30*, 631.
[15] S. Yamashita, K.-I. Miyamoto, M. Iguchi, M. Zeze, *ISIJ Int.* **2003**, *43*, 1858.
[16] J. Mandal, S. Patil, M. Madan, D. Mazumdar, *Metall. Mater. Trans. B* **2005**, *36*, 479.
[17] N. Mazumdar, A. Mahadevan, M. Madan, D. Mazumdar, *ISIJ Int.* **2005**, *45*, 1940.
[18] S. P. Patil, D. Satish, M. Peranandhanathan, D. Mazumdar, *ISIJ Int.* **2010**, *50*, 1117.
[19] N. Kochi, K. Mori, Y. Sasaki, M. Iguchi, *ISIJ Int.* **2011**, *51*, 1755.
[20] A. N. Conejo, S. Kitamura, N. Maruoka, S.-J. Kim, *Metall. Mater. Trans. B* **2013**, *44*, 914.
[21] A. M. Amaro-Villeda, M. A. Ramirez-Argaez, A. N. Conejo, *ISIJ Int.* **2014**, *54*, 1.
[22] M. S. C. Terrazas, A. N. Conejo, *Metall. Mater. Trans. B* **2015**, *46*, 711.
[23] S. Joo, R. I. L. Guthrie, *Metall. Trans. B* **1992**, *23*, 765.
[24] D. Mazumdar, R. I. L. Guthrie, *ISIJ Int.* **1995**, *35*, 1.
[25] M. Zhu, T. Inomoto, I. Sawada, T. Hsiao, *ISIJ Int.* **1995**, *35*, 472.
[26] M. Zhu, I. Sawada, N. Yamasaki, *ISIJ Int.* **1996**, *36*, 503.
[27] K.-S. Lee, W.-O. Yang, Y.-G. Park, K.-W. Yi, *Met. Mater. Int.* **2000**, *6*, 461.
[28] J. Anu, J. Lage, S. Dong-Yuan, *Scand. J. Metall.* **2001**, *30*, 242.
[29] D. Mazumdar, R. Yadav, B. B. Mahato, *ISIJ Int.* **2002**, *42*, 106.
[30] J. Aoki, B. G. Thomas, J. Peter, K. Peaslee, *AISTech 2004*, Assoc. Iron Steel Technology, Nashville, TN **2004**.
[31] M. Madan, D. Satish, D. Mazumdar, *ISIJ Int.* **2005**, *45*, 677.
[32] S. Ganguly, V. Singh, S. Chakraborty, *ISIJ Int.* **2006**, *46*, 1731.
[33] F. D. Maldonado-Parra, M. A. Ramírez-Argáez, A. N. Conejo, C. González, *ISIJ Int.* **2011**, *51*, 1110.
[34] S. W. P. Cloete, J. J. Eksteen, S. M. Bradshaw, *Miner. Eng.* **2013**, *46–47*, 16.
[35] K. Nakanishi, J. Szekely, C. Chang, *Ironmaking Steelmaking* **1975**, *2*, 115.
[36] S. Asai, T. Okamoto, J.-C. He, I. Muchi, *Trans. ISIJ Int.* **1983**, *23*, 43.
[37] M. Sano, K. Mori, *Trans. ISIJ Int.* **1983**, *23*, 169.
[38] S. Taniguchi, M. Ohmi, S. Ishiura, *Trans. ISIJ Int.* **1983**, *23*, 571.
[39] Z. Liuyi, *Steel Res. Int.* **1996**, *67*, 466.
[40] Z. Liuyi, O. Franz, *Steel Res. Int.* **1999**, *70*, 128.
[41] O. Franz, Z. Liuyi, H. Christian, L. Jürgen, *Steel Res. Int.* **2000**, *71*, 381.
[42] Z. Liuyi, O. Franz, *Steel Res. Int.* **2000**, *71*, 141.
[43] H. Duan, L. Zhang, B. G. Thomas, A. N. Conejo, *Metall. Mater. Trans. B* **2018**.
[44] H. Duan, L. Zhang, *The Eighth China-Korea Joint Symposium on Advanced Steel Technology*, Chongqing, China, June **2016**.
[45] L. Zhang, H. Duan, *The 5th Int. Conf. on Process Development in Iron and Steelmaking*, Lulea, Sweden, October **2016**.
[46] S. A. Morsi, A. J. Alexander, *J. Fluid Mech.* **1972**, *55*, 193.